



A Comparison Study of Turbulence Models in RANS Simulations of Rotor 67

Nathan Spotts* and Xinfeng Gao†

*Computational Fluid Dynamics and Propulsion Laboratory
 Colorado State University, Fort Collins, CO 80525, USA*

We present a numerical investigation of turbulence models applied to Reynolds Averaged Navier-Stokes (RANS) simulations of the transonic flow in NASA Rotor 67. The main objective of the present work is to evaluate the capability and performance of these turbulence models for their application to turbomachinery flows. Such flows are often characterized by features including complex shock systems, tip vortex-shock interactions, strong streamline curvature, secondary flows, flow separations, shock-wave boundary layer interactions, and system rotation. To better understand turbulence modeling of flows with these characteristics, we studied six turbulence models, ranging from simple one-equation algebraic model to a seven-equation second moment closure. Detailed results and validation using four of the selected eddy-viscosity closures are presented, while numerical convergence could not be achieved with the remaining two models. The results indicate that turbulence modeling has significant effects on aerodynamic performance predictions, predictions of boundary layer flows, and on convergence of simulations for operating points near the stall condition. The influence of the investigated turbulence models on flow outside of the boundary layers and within the blade passage has been found to be minimal. The one-equation Spalart-Allmaras and the two-equation Shear Stress Transport (SST) models have been shown to converge near the stall condition and provide reasonable results, while two-equation $k - \epsilon$ closures are numerically less stable near the stall condition.

In CFD simulations for engineering proposes, a balance must be found between performance, computational expense, and usability. This study provides important guidance on selection criteria for turbulence models for application to rotating flows in aerospace propulsion systems.

I. Introduction

NUMEROUS experimental and numerical studies have shown that rotation and/or streamline curvature can substantially modify both the mean flow field and the turbulence intensity and structure.¹⁻⁷ Among turbulence models, second-moment models appear to account for rotation effects due to the production terms in the model. However, their application to practical engineering flows is often restricted due to the computational expense and stiffness. Although two-equation turbulence models are frequently adopted in RANS simulations of engineering flows for less computation cost, it is the common belief that these models are independent of imposed system rotation. Over the past three decades, much research effort has been made to sensitize RANS models to non-inertial effects. For example, adding ad hoc rotation dependent terms to the dissipation rate transport equation, although not rigorous, improves the predictions of turbulent flows in non-inertial frames. The present investigation is not intended to study different approaches to sensitize turbulence models to rotation. Rather, we focus on conducting a systematic computational survey of a range of turbulence models from the one-equation algebraic model to the seven-equation second moment closure mode, through the application of these models to simulations of a rotating flow representative of that encountered in aerospace propulsion systems, thus providing a performance comparison. In this work, we select six turbulence models for RANS simulations of rotating flows in Rotor 67, including the one equation Spalart-Allmaras model,⁸ the two-equation realizable $k - \epsilon$ model,^{9,10} the two-equation non-linear (cubic)

*Graduate Research Assistant, Email: nspotts@engr.colostate.edu, Student Member AIAA

†Assistant Professor, Email: xinfeng.gao@colostate.edu, Member AIAA

$k-\epsilon$ model,¹¹ the two-equation SST model,⁸ the Hellsten quartic $k-\omega$ model,³ and the seven-equation second moment closure model.^{12,13} For completeness, the models are summarized in detail in Appendix VII.A.

Flows for the Rotor 67 configuration have been investigated both computationally and experimentally by many parties in the past 3 decades. While many numerical investigations of the flow have been completed, no known studies have studied the effects of turbulence models by direct comparison of results obtained on identical grids and with the same CFD solver. However, previous numerical investigations have greatly elucidated both the flow physics present in Rotor 67 and the effectiveness of various CFD methods in capturing these physics. Early viscous simulations by Chima¹⁴ resolved the flow remarkably well using a node-centered, second-order finite-difference scheme, and employing a modified Baldwin-Lomax turbulence model. The CFD predictions agreed well in almost all regards with the detailed experimental data of Strazisar *et al.*¹⁵ Fan performance and radial profiles of stagnation quantities were predicted accurately, while static pressure and flow angle showed some disagreement with experimental data. Location and strength of shocks were over-predicted near the stall point, but predicted accurately near peak efficiency. Wake profile predictions were much deeper than those observed experimentally, but the wakes' locations and spreading were in good agreement with the experiment. Viscous simulations were conducted by Hah¹⁶ who studied the flow in Rotor 67 with a focus on shock-boundary layer interaction, radial transport, and wake development. A two-equation $k-\epsilon$ turbulence model, modified to include low Reynolds number effects, was used. Arima also used a low Reynolds number formulation of the standard $k-\epsilon$ model, obtaining similar results to Hah and Chima, but with improved agreement of radial profiles with experimental data.

Recently, investigations of the near stall conditions and shock-wake boundary layer interaction (SWBLI) were presented by Grosvenor^{17,18}. These simulations employed the one-equation Spalart-Allmaras turbulence model in a modern density-based compressible RANS finite-volume method (FVM) solver with added artificial dissipation. The Spalart-Allmaras turbulence model was chosen for these simulations because of its accurate predictions of flow features including boundary layer development, shock-wave boundary-layer interaction, and separation in diffusing flows. The model was also noted to be computationally efficient, robust, and have minimal grid resolution requirements. Follow-on simulations by Grosvenor used high resolution RANS nonlinear harmonics methods to study tip-injection physics. The Spalart-Allmaras model was again used. Fidalgo *et al.*¹⁹ conducted full-annulus, unsteady CFD simulations of the Rotor 67 stage in the presence of circumferential inlet distortion. An unsteady RANS, compressible, unstructured FVM solver with a Roe upwind scheme and dual time stepping. The Spalart-Allmaras turbulence model was employed. Time-averaged solutions of the flow field, independent of the blades, was calculated using Adamczyk's method.²⁰ Fidalgo's work elucidated the physics of fan-distortion interaction.

Next, we will describe the geometric configuration and computational grids used for the present study. Details of the CFD solver, solution methods, and post-processing are described in Section III. Finally, we present and discuss the results. Conclusions are drawn and future work is proposed.

II. Computational Model of Rotor 67

II.A. Geometry

As previously stated, the geometry studied herein is that of NASA Rotor 67, a low aspect ratio transonic fan. The rotor is comprised of 22, multiple-circular-arc blades and is the first stage rotor of a two stage fan designed at NASA Lewis.²¹ Numerous references provide descriptions of the rotor geometry^{22 21 15 23 24 25}. Characteristic parameters of the rotor design are listed in Table 1.

To obtain a geometric representation suitable for grid generation, non-uniform rational B-spline surfaces were created from discrete geometry received from NASA in Plot3D format. A rolling ball fillet with a radius of 1.78 mm was created at the blade-hub interface, a feature consistent with the geometry presented by Strazisar *et al.*¹⁵ With the intention of decreasing the interaction of the blades with inlet and outlet numerical boundary conditions, constant diameter duct sections were added upstream and downstream of the flow path defined by the geometry received from NASA. Representative rotor blade sections are illustrated for three spanwise locations, hub, midheight, and tip, in Figure 1 and Figure 2¹⁵ shows the blade geometry on the meridional plane.

Table 1: Characteristic parameters for the rotor-alone operating at 100% of design speed

Number of blades	22	Inlet tip relative Mach number	1.38
Rotation speed	16043 rpm	Rotor aspect ratio	1.56
Mass flow	33.25 kg/s	Rotor solidity at hub	3.11
Pressure ratio	1.63	Rotor solidity at tip	1.29
Isentropic efficiency	0.92	Tip diameter at inlet	51.4 cm
Rotor tip speed	429 m/s	Tip diameter at exit	48.5 cm
Tip clearance	1.006 mm	Mean hub/tip radius ratio	0.375

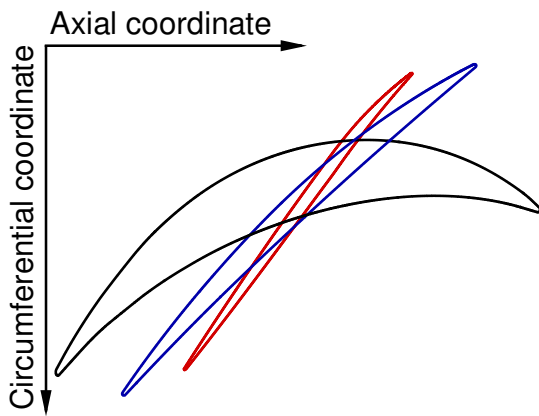
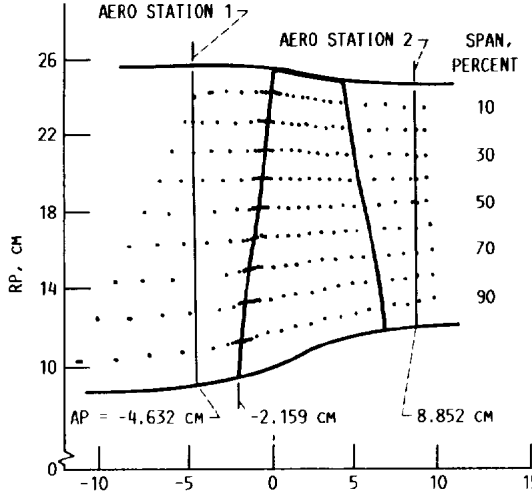


Figure 1: Representative blade sections of the rotor at three spanwise locations: hub (black), midspan (blue) and shroud (red).

Figure 2: Meridional view of test fan rotor showing laser anemometer and aerodynamic survey locations¹⁵

II.B. Computational Grids

Multi-block, structured grids were used for all computations because of both the accuracy afforded by the implicit alignment of cell faces with the flow in turbomachinery simulations and their ability to be highly controlled with regard to cell stretching ratios. All meshes were generated with the commercial software Pointwise. Particular attention was paid to near-body cell quality, to minimize error in the resolution of boundary layers. Multi-block topologies were chosen such that highly orthogonal grids were obtained, despite the complex geometry. All geometric features of the rotor were reproduced in the grids, including the 1 mm tip clearance gap and 1.78 mm fillet at the hub-blade interface.

A series of three grids, with widely varying cell counts, were generated so that the dependence of solutions upon grid resolution could be assessed. The grids are referred to herein as coarse, medium, and fine. To generate this series of grids, the finest grid in each series was constructed with Pointwise, output to Plot3D format and uniformly coarsened successively using a utility within CFD++.²⁶ Wall spacing for grids were chosen such that resultant first y^+ values were mostly less than 1, even on the coarsest grid. Due to the uniform coarsening, stretching ratios for fine grids were small compared to the coarsened grids. Representative grid metrics are shown in Table 2. Each grid considered a single, periodic passage of the geometry, and the periodic boundaries were point-matched to each other. The grid quality metrics observed most closely were equiangle skewness and stretching ratios, with equiangle skewness kept strictly below 0.87. An O-J topology was chosen for the rotor in order to maximize cell orthogonality, minimize cell counts and, minimize aspect ratios away from wall boundaries. While this topology is not such that the rotor wake may be well resolved with clustering of the grid cells, as would be the case for O-H or O-C topologies, the current study is part of a greater work in which sliding-mesh URANS simulations of the full-annulus Rotor

67 stage have been performed, thus precluding O-H or O-C topologies, which would result in interpolation errors at the sliding boundary between the rotor and stator due to disparate cell sizes. Figure 3a shows the O-J topology of the coarse rotor grid near the midspan. The tip clearance region was fully meshed, with a O-H topology ("butterfly" mesh). The grid in the vicinity of the rotor's tip, near the leading edge, is shown in Figure 3b, with the surface grid of the rotor shaded blue, volume grids shaded red, and a portion of the shroud shaded green. The fillet was fully meshed as shown in Figure 3c. The periodic boundary of the coarse rotor grid is shown on the meridional plane in Figure 3d.

Table 2: Representative grid metrics

Cells	LE/TE Cells	Blade Chord Cells	Tip Gap Cells	Total Radial Cells	y_1^+ , max	Stretching Ratio
6.62×10^5	12	80	30	95	1.6	1.45
5.29×10^6	24	160	60	190	0.8	1.2
4.24×10^7	48	320	120	380	0.4	1.1

III. CFD Simulation Methods

III.A. CFD Solver and Cases Setup

The solver used for all simulations was the CFD++ solver from Metacomp Technologies.²⁶ CFD++ is an unstructured solver which uses a second-order, upwind, finite-volume method with an HLLC approximate Riemann solver to find solutions to the Reynolds-Averaged Navier-Stokes equations using Gauss-Seidel relaxation accelerated with algebraic multi-grid. A number of turbulence models are available in the solver, and we investigated the six models as summarized in Appendix VII.A.

Initial conditions were specified with a uniform velocity field of 200 m/s in the axial direction and standard atmospheric values of pressure and temperature. Following cases were often initialized with previous solutions in order to minimize the cases' run times. The turbulence boundary condition at the inlet was used also as the initial turbulence condition for the whole computational domain. It was calculated using the following parameters: 2% turbulence, 0.04 m length scale ($\sim 1/4$ of the annular passage span at the inlet), and 200 m/s velocity. This results in $\mu_t/\mu = 1177.415$.

Stagnation quantities were prescribed at the inlet boundary, and flow was assumed to be normal to the faces on the inlet boundary. Because experimental data was not available at the location of the inlet boundary (due to the constant radius upstream extension of the geometry), uniform inlet conditions were prescribed, resulting in a slightly thinner boundary layer profile at the experimental station just upstream of the rotor than was likely present in the experiment. Static pressure with radial equilibrium was prescribed at the outlet of internal flow cases, and the back pressure was iterated during the calculations to achieve the desired mass flow rate. Twelve operation points were simulated with each turbulence model, in order to establish an operating speed-line. The normalized mass flow rates of the operating points were chosen consistently for each model based on the results of cases known to be at the choked flow condition.

Convergence of the steady-state simulations was measured by observing the stability of the fan's pressure ratio and mass flow rate over the final iterations of a given case, as well as the levels of normalized residuals present at the end of the simulation. Generally, at least 4-order reduction in the normalized residuals of the calculations was achieved.

III.B. Post-Processing Methods

Analysis of data from single-passage CFD solutions was performed to obtain the aerodynamic performance of the rotor as well as pitch-averaged spanwise profiles of important flow quantities. Additionally, relative Mach number for blade-to-blade lines at constant chord and streamwise lines at constant pitch was extracted for direct comparison to experimental laser anemometry data. The spanwise profiles, constant chord, and constant pitch lines were extracted for two operating points. An operating point near peak efficiency and an operating point near the stall condition. These operating points are defined by the mass flow rate through

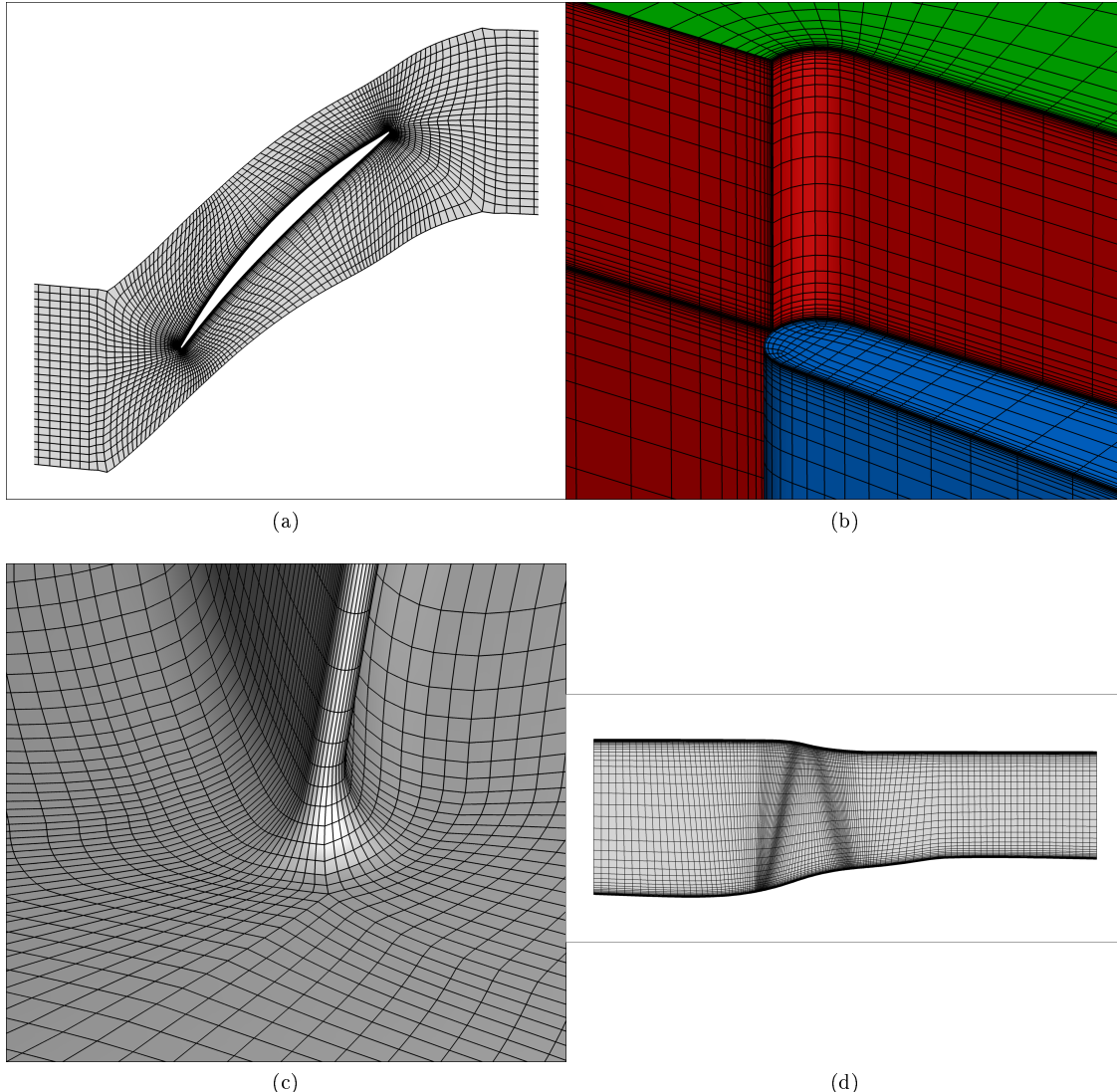


Figure 3: Coarse rotor grids. (a) Blade-to-blade grid near the midspan, (b) grid in tip gap region, (c) surface grid in fillet region (d) periodic grid on meridional plane

the rotor, normalized by the rotor's choked mass flow rate, and were defined by Strazisar *et al.* as being at 0.989 and 0.924, for the peak efficiency and stall conditions, respectively. The locations of aerodynamic measurements stations as well as constant chord and constant pitch lines are shown in Figure 2. The extraction of all data was performed by linearly interpolating the CFD solutions onto structured grids with Tecplot. Structured grids for data interpolation and processing were generated to match the CFD grids as closely as possibly with respect to cell spacings, in an effort to minimize error in the interpolation. Solutions on structured grids were then post-processed to obtain the needed plots. Performance calculations and averaging were done with MATLAB. Data transfer between Tecplot and MATLAB was accomplished with a bash script written for that purpose. Bash scripts were used to automate all post processing procedures to ensure efficient and consistent post processing of the data.

III.C. Radial Profiles

Radial profiles of total pressure, total temperature, and relative flow angle were produced for each single-passage CFD simulation. Station locations at which radial profiles were obtained were those used by Strazisar *et al.* for aerodynamic surveys. These stations are shown in Figure 2. The flow field at each station location

was averaged in the circumferential direction using a mass flow rate weighted average. The mass flow rate weighted averaging was performed on data interpolated to structured grids with lines of constant radius. The averaging was performed across all cells of a given radius (N), using Equations 1 - 3, where A is the cell area, and U is the velocity normal to the cell face. Only scalar quantities were able to be averaged in this manner, therefore, the relative flow angle (β) was calculated from vector quantities before averaging.

$$\bar{P}_0 = \frac{\sum_{n=1}^N P_{0n} \rho_n U_n A_n}{\sum_{n=1}^N \rho_n U_n A_n} \quad (1)$$

$$\bar{T}_0 = \frac{\sum_{n=1}^N T_{0n} \rho_n U_n A_n}{\sum_{n=1}^N \rho_n U_n A_n} \quad (2)$$

$$\bar{\beta}_0 = \frac{\sum_{n=1}^N \beta_{0n} \rho_n U_n A_n}{\sum_{n=1}^N \rho_n U_n A_n} \quad (3)$$

III.D. Aerodynamic Performance Calculations

Aerodynamic performance of the rotor was determined for each CFD simulation and the aerodynamic performance of the stage was also calculated for solutions involving both rotor and stator. Rake integrations were performed at the stations specified in the primary experimental reference¹⁵ and shown in Figure 2. The total pressure across the fan was calculated as $(\frac{P_{02}}{P_{01}})$ and the isentropic efficiency was calculated with Equation 4.¹⁵

$$\eta = \frac{\frac{P_{02}}{P_{01}}^{\frac{\gamma-1}{\gamma}} - 1}{\frac{T_{02}}{T_{01}} - 1} \quad (4)$$

Aerodynamic performance was calculated using rake data in order to allow for comparison to experimental data. Circumferentially averaged radial profiles, as described above, were linearly interpolated to the radial locations used in the experiment which were comprised of 9 survey locations between the hub and shroud. The data points at each station were then averaged to obtain a value at each station for total pressure and total temperature, which was again used to calculate aerodynamic performance. The radial distributions of total temperature were averaged with mass flow rate weighting, and the total pressure distributions were averaged with the energy average method used in reference .¹⁵ The total temperature average was consistent with Equation 2. The average of total pressure was performed using Equation 5, in which the total pressures are converted to their enthalpy equivalents and then mass averaged. In Equation 5, the ΔA is the incremental annulus area, which was taken directly from reference .¹⁵

$$\bar{P}_0 = \left[\frac{\sum_{n=1}^N P_{0n}^{\frac{\gamma-1}{\gamma}} \rho_n U_n (\Delta A_n)}{\sum_{n=1}^N \rho_n U_n (\Delta A_n)} \right]^{\frac{1}{\gamma-1}} \quad (5)$$

III.E. Flow Field Data Extraction for Comparison with Laser Anemometry Data

A structured grid with lines of constant pitch and constant chord, all at a constant spanwise percentage was used to extract flow field data for comparison with Laser Anemometry (LA) data. These grids had 1000 vertices in the streamwise direction and 200 vertices from blade-to-blade. The spanwise positions of the grids were obtained by projecting to a surface created from data presented by Strazisar *et al.*¹⁵ As stated previously, the convention defined by Strazisar *et al.*¹⁵ has been followed when referencing spanwise location, with 0% span being defined at the shroud. In order to avoid confusion, this convention is important to note, because modern convention defines the hub as being at 0% span .¹⁹ Furthermore, it is notable that the spanwise locations defined by Strazisar *et al.*¹⁵ were only calculated from the design streamlines at a number of discreet axial locations (i.e. rake measurement stations and the rotor's leading and trailing edges); between these points, straight-line interpolation was used. Locations of constant span lines are shown in Figure 2. Grids were generated at 10%, 30%, and 70% span from the shroud.

A schematic representation of lines of constant pitch and constant chord, for which relative Mach number data were extracted from CFD solutions and compared to LA data, is shown in Figure 4. Pitch within the

passage was determined by the circumferential coordinate at any given axial location. The suction surface of the blade was taken to be at 0% pitch, and the pressure surface of the contiguous blade was taken to be at 100% pitch. Outside of the passage, 0% and 100% pitch were taken to be at lines extended from the leading and trailing edges at the blade inlet and outlet angles, respectively. A schematic representation of a 50% pitch line is shown in 4. Chord was defined by the axial distance between the leading and trailing edges of the blade at a given span, with 0% chord being defined at the leading edge of the blade and 100% chord being defined at the trailing edge of the blade. A schematic representation of constant chord lines outside of the blade passage is shown in 4.

Because the interpolation grids had lines of constant pitch, they were not entirely within the domain of the computational grids. Interpolation required repeated rotation by the periodicity of the blade; then interpolating onto the section of the interpolation grid contained within the computational grids. Streamwise and chordwise locations of each grid point were calculated using a Tecplot macro and added to the interpolation grid as variables. Indices corresponding to the desired constant pitch or constant chord line were then extracted, and plotted against LA data. This procedure was only applied for single-passage solutions.

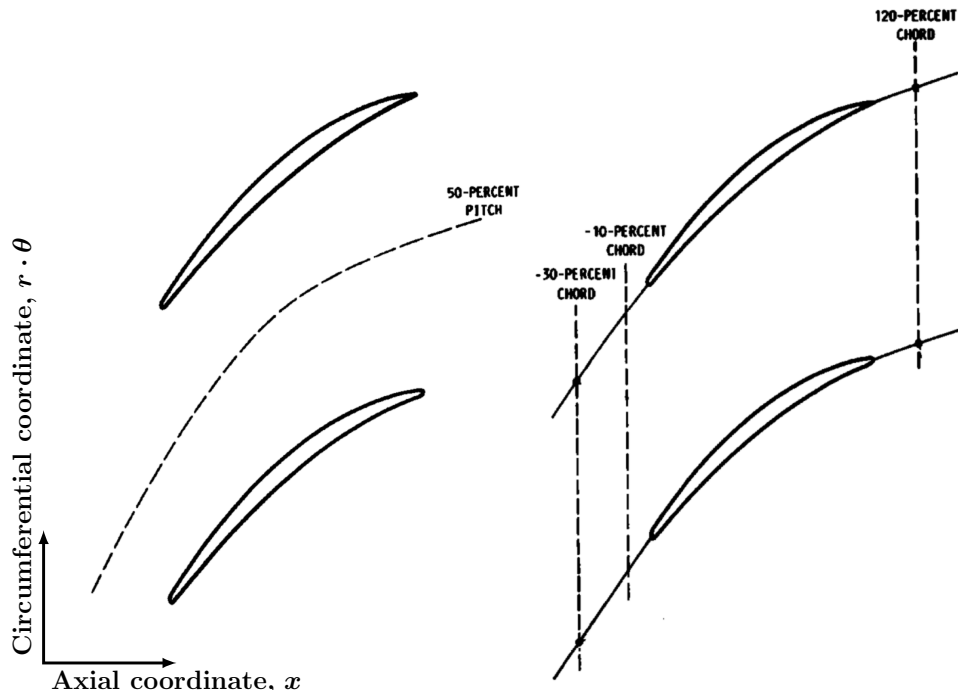


Figure 4: Schematic representations of constant pitch lines (left) and constant chord lines (right) used to plot data in streamwise and blade-to-blade directions, respectively. Figure adapted from ¹⁵

IV. Results and Discussions

Results were obtained using the four turbulence models previously discussed: the Spalart-Allmaras (Eqs. 6-7), realizable $k - \epsilon$ (Eqs. 8-9), cubic $k - \epsilon$ (Eqs. 10-11), and SST (Eqs. 12-13) models. Results from these models are presented below along and comparisons are made to experimental data from Strazisar *et al.*¹⁵ While simulations were completed using the seven-equation second-moment model (Eq. 14), and the Hellsten quartic $k - \omega$ model (Eqs. 15-16), acceptable levels of convergence were not obtained with these models. Therefore, detailed results are not presented for these models. All simulations for comparison of turbulence models were completed using the medium grid described previously (5.29×10^6 cells). A grid refinement study was completed and a grid independence was reasonably achieved for RANS-type simulations, as shown in Appendix VII.B.

The aerodynamic performance of the fan, as calculated from simulations using the various turbulence models, is shown in Figure 5, which presents isentropic efficiency (top) and fan pressure ratio (FPR) (bottom).

The turbulence modeling has a significant effect on efficiency. The Spalart-Allmaras model predicts the lowest efficiency, which is closest to the experimental values over most of the operating range. None of the models predict the sharp decrease in efficiency at slightly lower mass flow rates than that of the peak efficiency point. All of the models capture the trend in the efficiency curve accurately and the peak efficiency points are at nearly identical mass flow rates, which were slightly lower than that found experimentally. Notably, the $k - \epsilon$ models did not converge at the experimentally determined near stall condition. Therefore in the detailed comparisons of results at the near stall condition which follow, only the Spalart-Allmaras and SST models are presented. All four models converged at the peak efficiency point, so detailed comparisons of model performance at this point do not exclude any of the four models.

Predictions of the FPR are less effected by the turbulence modelling, with all of the models yielding results which agree very closely with the experimental data. The SST model predicts slightly higher FPR than do the other models, as the stall condition is approached.

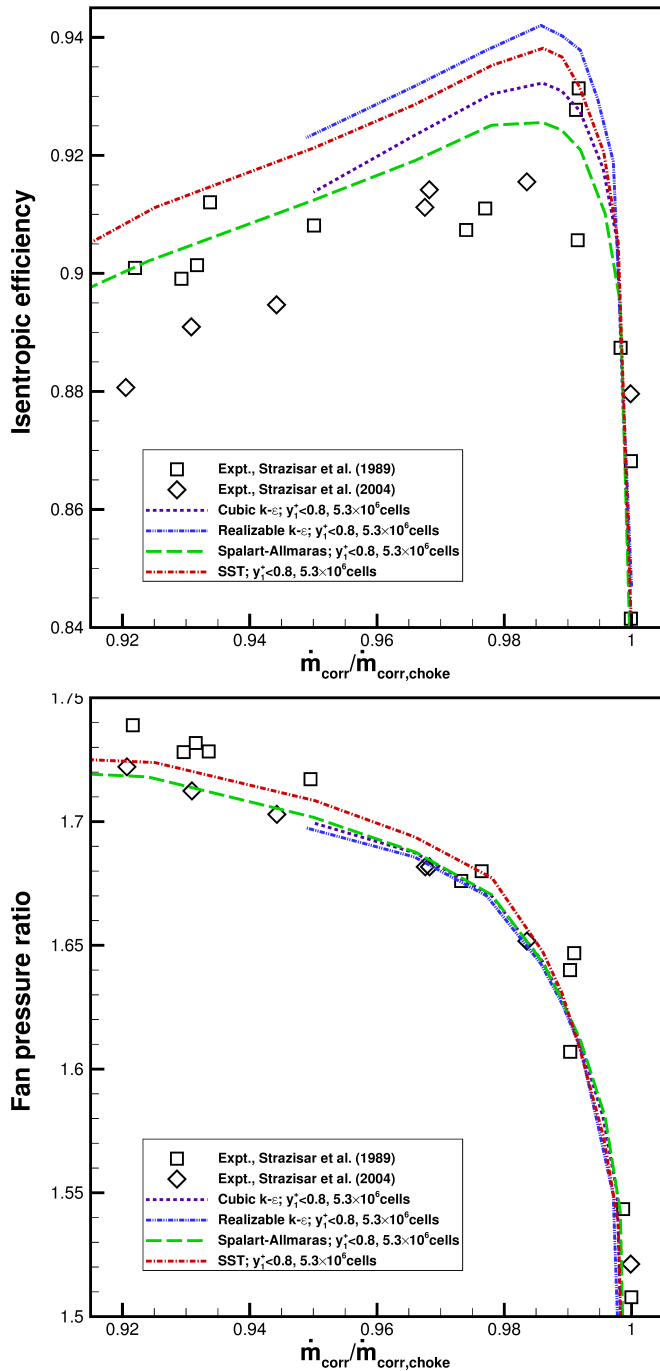


Figure 5: Efficiency and FPR

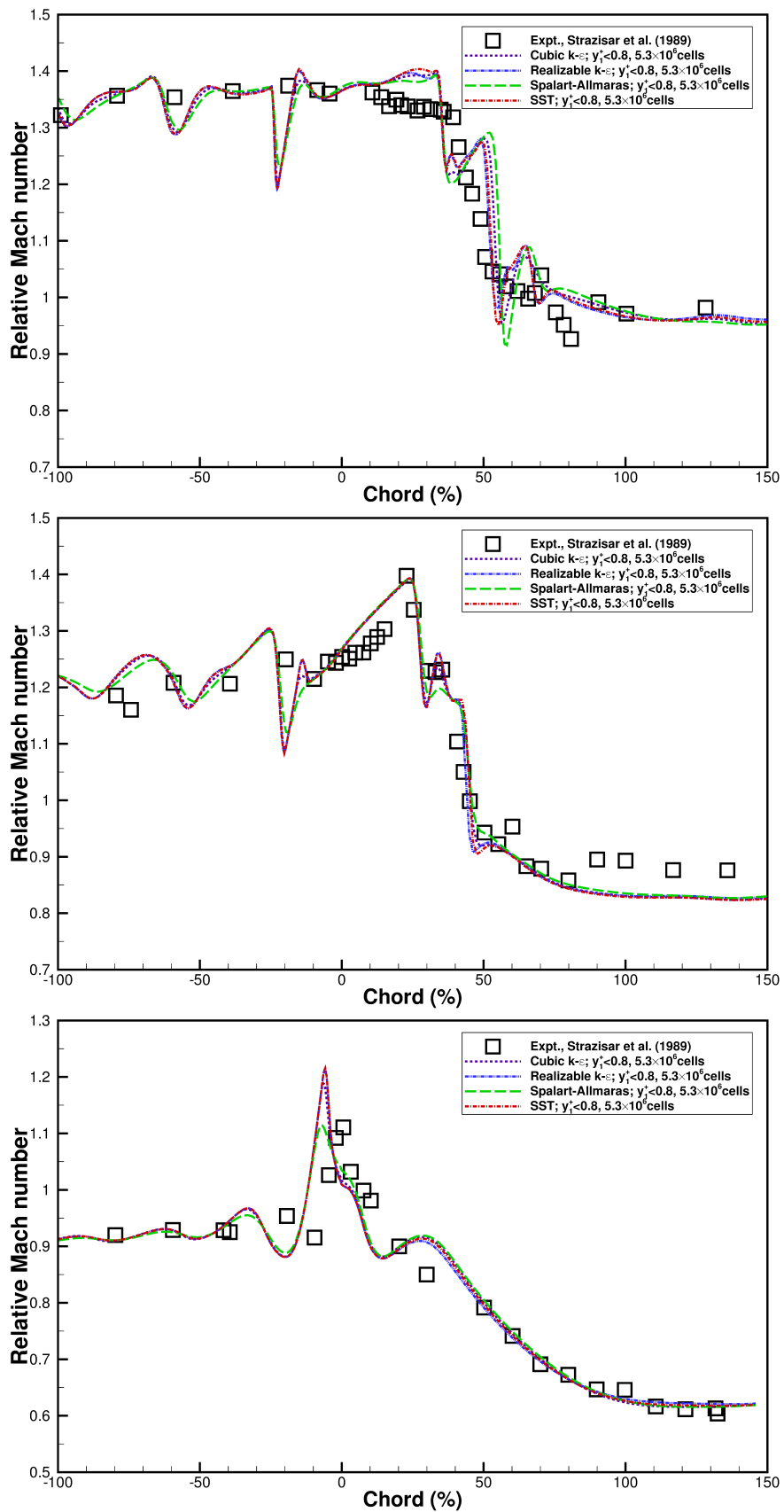


Figure 6: Relative Mach number at 90% span (top), 70% span (middle), and 30% span (bottom) from the hub and at 50% pitch, for the rotor alone operating near peak efficiency.

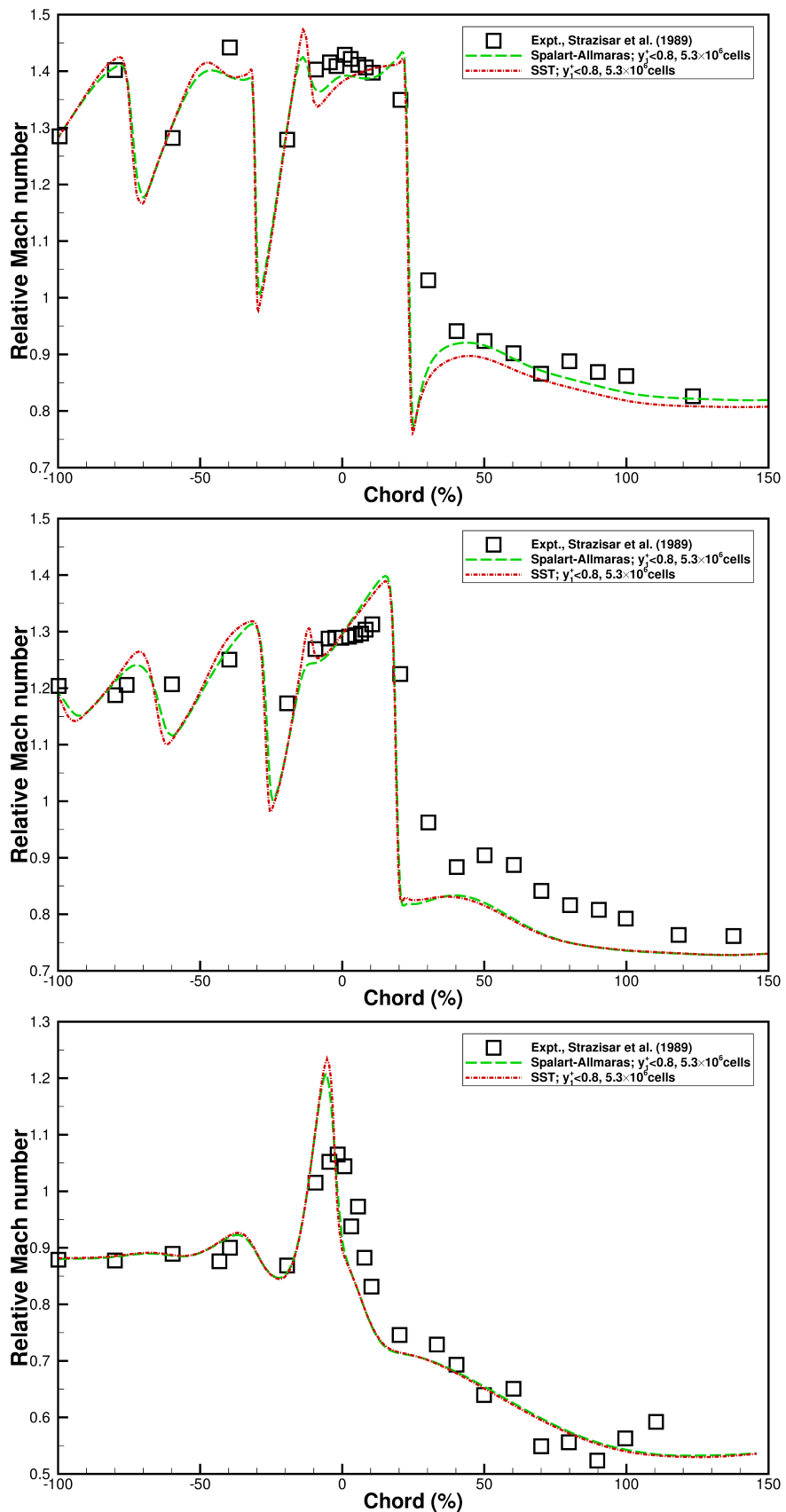


Figure 7: Relative Mach number at 90% span (top), 70% span (middle), and 30% span (bottom) from the hub and at 50% pitch, for the rotor alone operating near stall.

Figures 6 and 7 show results in the streamwise direction at 50% pitch for the rotor alone operating near peak efficiency point and near stall, respectively. In both figure, plots of relative Mach number at 90%, 70%, and 30% span from the hub are shown in Figures 6 at the top, middle, and bottom, respectively. In the figure, experimental data is also presented for comparison. The flow along these 50% pitch lines, away from the blade surfaces, appears to be minimally effected by the choice of turbulence models. Shock locations are predicted accurately by all models. The Spalart-Allmaras model appears to slightly dissipate the shocks, as can be seen by the lower magnitude of the relative Mach number line plots at inflection points.

Radial profile of total pressure, total temperature, static pressure, and absolute flow angle, at a station downstream of the rotor, are presented in Figures 8 and 9. Figure 8 shows the spanwise distributions for the rotor operating near peak efficiency and Figure 9 shows the same for the rotor operating near the stall point. Near the best efficiency point, the variation of predictions between the models is small and the agreement of stagnation quantities and flow angle with experimental data is good. The realizable $k - \epsilon$ matches the slightly lower total pressure and total temperature seen in the experimental data at approximately 40% span better than do the other models. All of the model underpredict the total pressure near the tip. The static pressure predictions do not agree well with the experimental data, however, static pressure was not directly measured in the experiment, but rather was calculated from other measured quantities, possibly introducing some uncertainty.

Radial profiles for an operating condition near stall exhibit a strong dependence on the turbulence model. This is most apparent in the radial profile of total pressure in Figure 9, where predictions at spans less than 40% are very different between the Spalart-Allmaras and the SST model. This may be due to radial flow induced by increased blockage from separation near the trailing edge of the blade, that can be seen from surface streamlines on the blade. The SST model predicts the trend in total pressure over the span well, while the Spalart-Allmaras model does not capture the higher total pressure at approximately 30% span.

Surface streamlines on the suction surface of the blade are shown in Figure 10. From the plots it can be seen that the influence of the turbulence modeling on the flow within the boundary layers is significant, especially near the trailing edge of the blade and at spanwise locations near the hub. At the operating condition near stall, the SST model predicts a much large separation bubble in this region. Consequently, greater radial flow is observed forward on the blade than is seen from the Spalart-Allmaras result. The shock induced boundary layer separation near the tip appears similar between the models, although it may extend to a lower span in the simulation using the SST model. At the operating condition near peak efficiency, the trends are similar between the predictions from the four models. The shock induced separation is again relatively unaffected by the choice of turbulence model. However, differences may be noted in the separated regions along the trailing edge, near the hub. The Spalart-Allmaras model predicts the smallest vorticle separation bubble of the models, but with a significant region of separation extending up the blade very close to the trailing edge. The realizable $k - \epsilon$ model also predicts this separation extending upwards on the blade, but does not show a vortex formation near the hub.

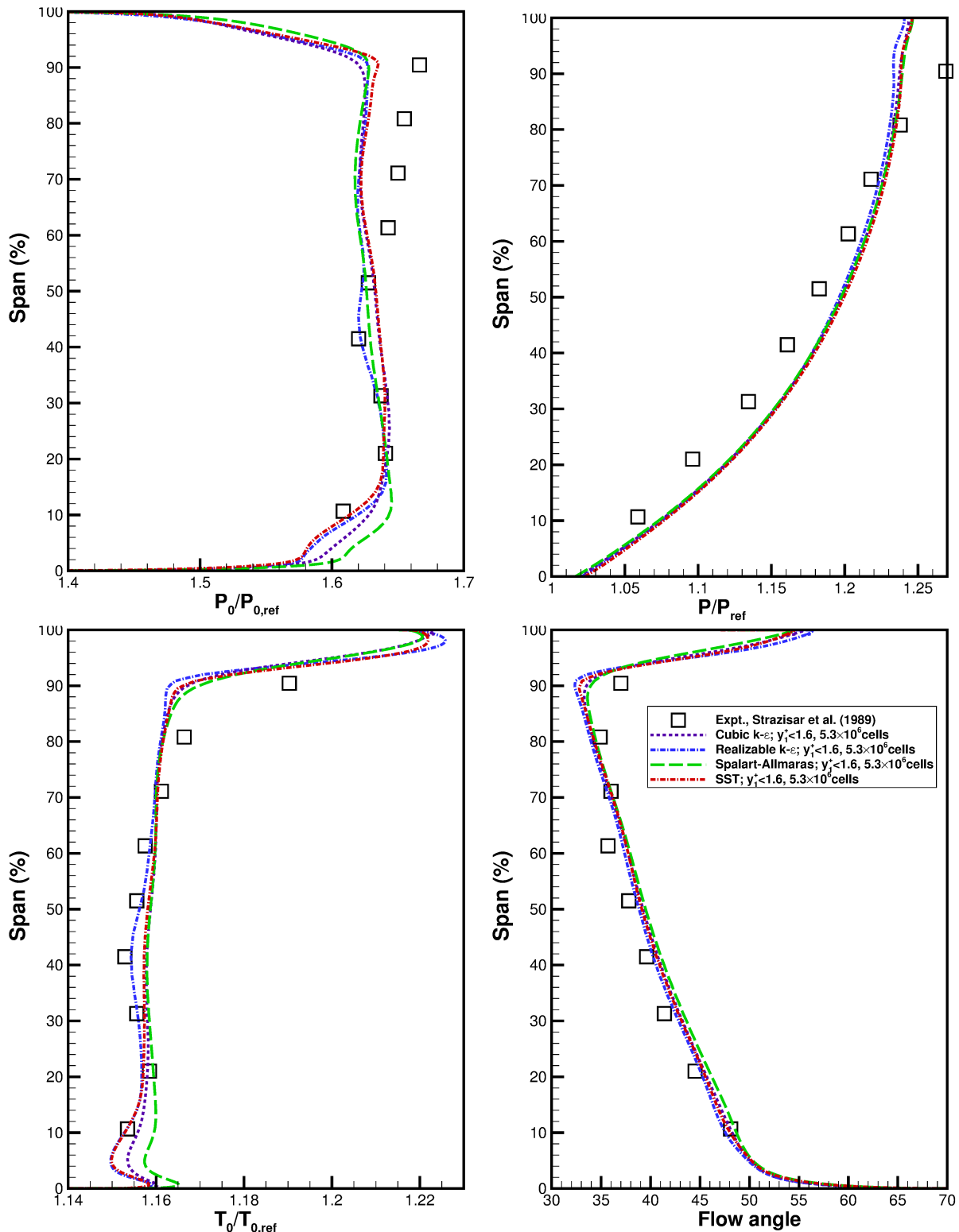


Figure 8: Spanwise distributions of total pressure (top-left), total temperature (top-right), static pressure (bottom-left), and exit flow angle (bottom-right) for the rotor alone operating near peak efficiency

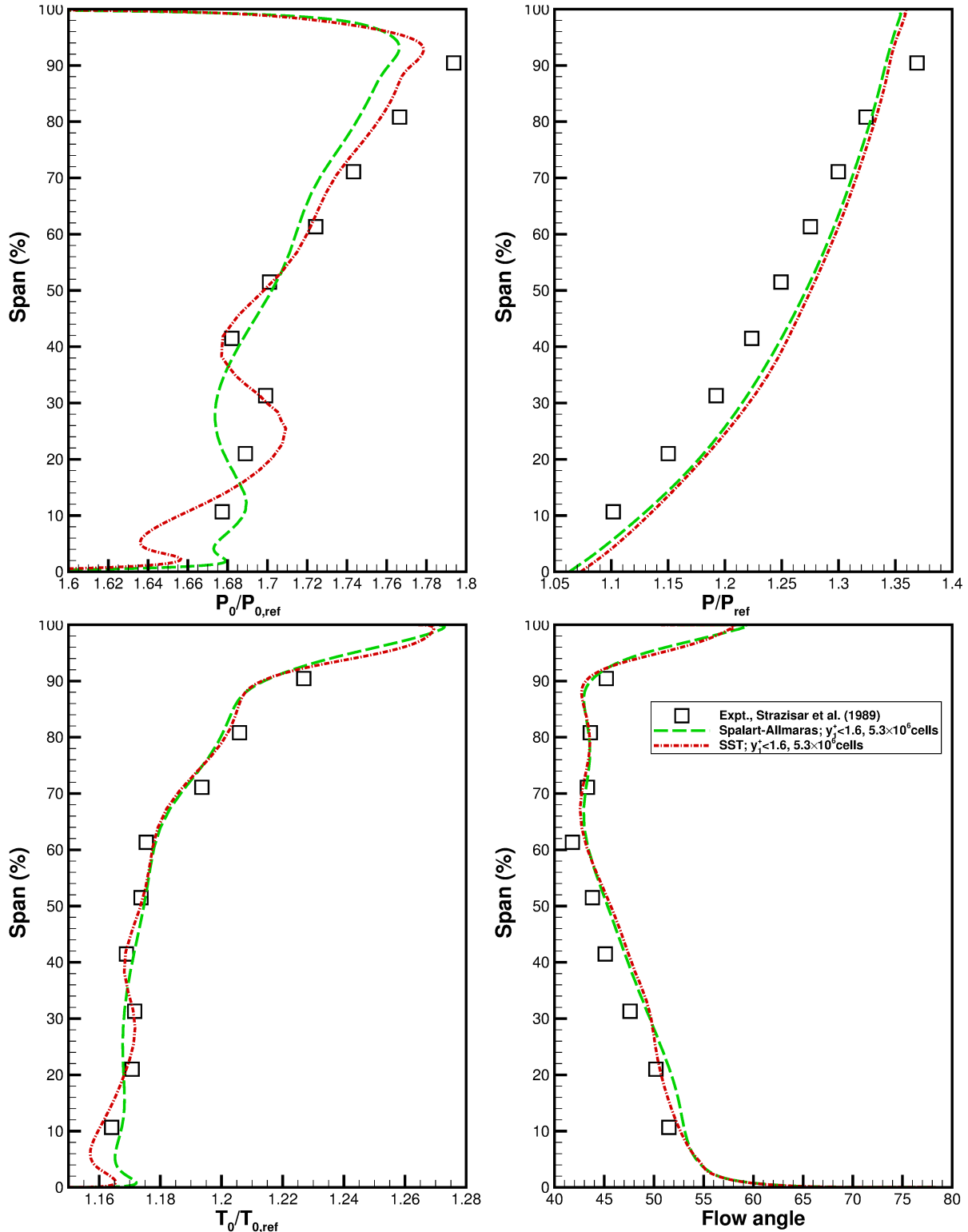


Figure 9: Spanwise distributions of total pressure (top-left), total temperature (top-right), static pressure (bottom-left), and exit flow angle (bottom-right) for the rotor alone operating near peak efficiency

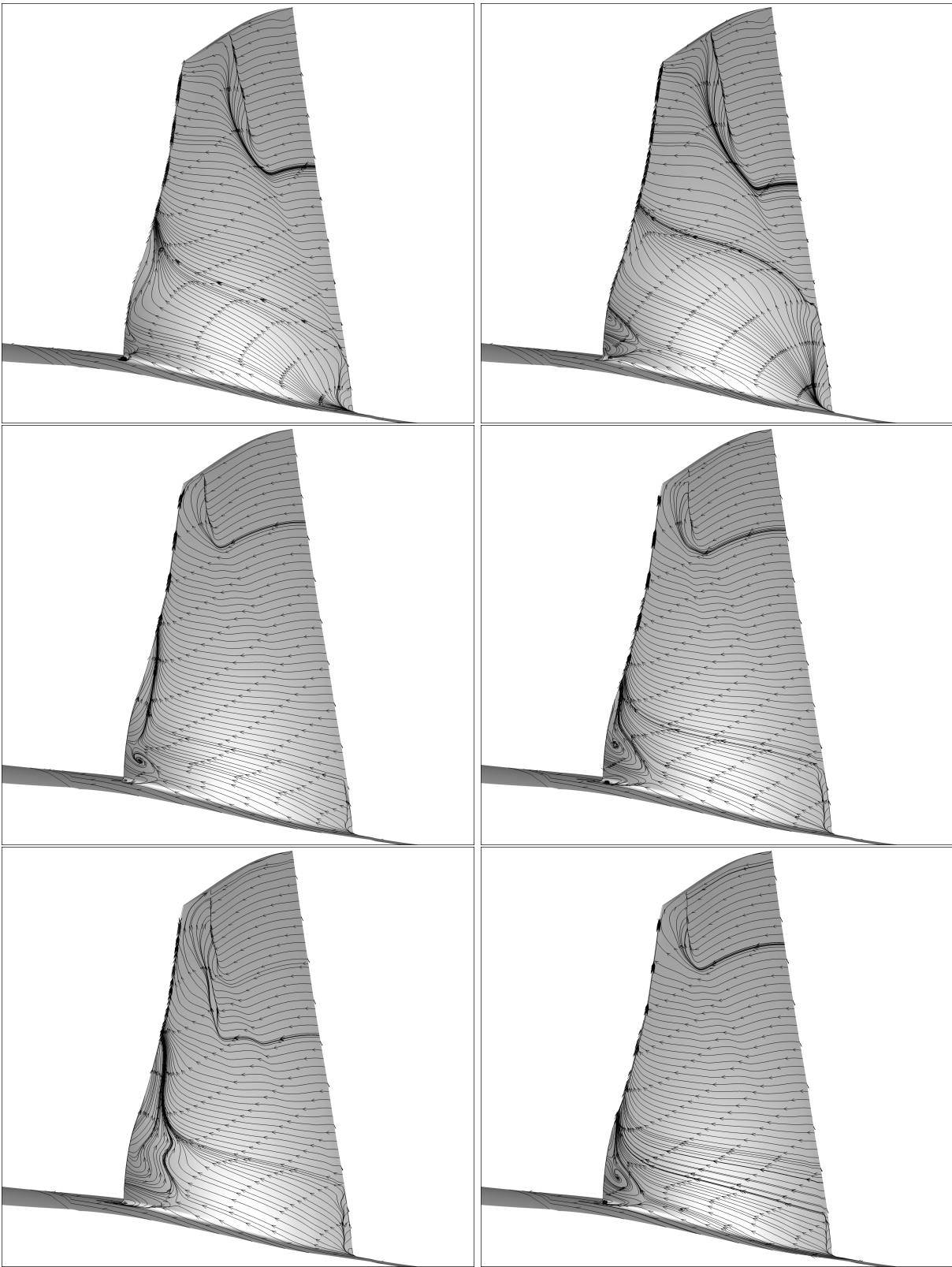


Figure 10: Surface streamlines for the rotor operating near peak efficiency and near stall. Results from simulations near stall using the Spalart-Allmaras (upper-left), SST (upper-right); near peak efficiency using the Spalart-Allmaras (middle-left), SST (middle-right), realizable $k - \epsilon$ (lower-left), and cubic $k - \epsilon$ models (lower-right).

V. Conclusions

We investigated RANS simulations with turbulence models ranging from simple one-equation algebraic model to the seven-equation second moment closure mode in rotating flow encountered in the aerospace propulsion system. The present work is to evaluate the capability and performance of these turbulence models for their application to turbomachinery flows featuring adverse pressure gradient, flow separation, secondary flow recirculation, tip clearance flow, shock-wave boundary layer interaction, rotation and curvature effect. To better understand turbulence modeling of the flow characteristics, we studied six turbulence models for RANS simulations of the flows in Rotor 67. The two-equation $k - \epsilon$ models exhibited less stability near the stall condition. Significant differences between the models' prediction were noted in radial profiles of stagnation quantities for operating conditions near stall. A strong influence of the models on the boundary layer flow was also observed from surface streamline plots, with the extents of separations in regions of adverse pressure gradients being effected by the turbulence modeling. Future work may include comparison of RANS results with time-averaged LES results.

VI. Acknowledgment

Research at the Colorado State University was supported by the Boeing company. We are grateful to Metacomp Technologies for their strong support. Parts of this work are adapted from a thesis submitted to the Academic Faculty of Colorado State University in partial fulfillment of the requirements for the degree of Master of Science in Mechanical Engineering

VII. Appendix

VII.A. Turbulence Models

- One equation Spalart-Allmaras model: the kinematic eddy viscosity, ν_T , is given by

$$\nu_T = \tilde{\nu} f_{\nu 1}. \quad (6)$$

The eddy viscosity, $\tilde{\nu}$, transport equation is modeled by

$$\frac{\partial \tilde{\nu}}{\partial t} + U_j \frac{\partial \tilde{\nu}}{\partial x_j} = c_{b1} \tilde{S} \tilde{\nu} - c_{w1} f_w \left(\frac{\tilde{\nu}}{d} \right)^2 + \frac{1}{\sigma} \frac{\partial}{\partial x_k} \left[(\nu + \tilde{\nu}) \frac{\partial \tilde{\nu}}{\partial x_k} \right] + \frac{c_{b2}}{\sigma} \frac{\partial \tilde{\nu}}{\partial x_k} \frac{\partial \tilde{\nu}}{\partial x_k}, \quad (7)$$

with closure coefficients and auxiliary relations as follows.

$$c_{b1} = 0.1355, c_{b2} = 0.622, c_{\nu 1} = 7.1, \sigma = 2/3, c_{w1} = \frac{c_{b1}}{k^2} + \frac{(1 + c_{b2})}{\sigma}, c_{w2} = 0.3, c_{w3} = 2, \kappa = 0.41,$$

$$f_{\nu 1} = \frac{\chi^3}{\chi^3 + c_{\nu 1}^3}, f_{\nu 2} = 1 - \frac{\chi}{1 + \chi f_{\nu 1}}, f_w = g \left[\frac{1 + c_{w3}^6}{g^6 + c_{w3}^6} \right]^{1/6} \chi = \frac{\tilde{\nu}}{\nu}, g = r + c_{w2}(r^6 - r), r = \frac{\tilde{\nu}}{\tilde{S} \kappa^2 d^2}.$$

The shear/strain rate tensor, S , and the rotation tensor, Ω , are defined by

$$\tilde{S} = S + \frac{\tilde{\nu}}{\kappa^2 d^2} f_{\nu 2}, \quad S = \sqrt{2\Omega_{ij}\Omega_{ij}}, \quad \Omega_{ij} = \frac{1}{2} \left(\frac{\partial U_i}{\partial x_j} - \frac{\partial U_j}{\partial x_i} \right),$$

where U is the freestream velocity. In above equations, d is the distance from the closest wall, σ is the non-equilibrium parameter, and κ is the Karaman constant.

- Two-equation realizable $k - \epsilon$ model: transport equations for turbulent kinetic energy, k , and the rate of dissipation of turbulent kinetic energy, ϵ :

$$\frac{\partial(\rho k)}{\partial t} + \frac{\partial(\rho k u_j)}{\partial x_j} = \frac{\partial}{\partial x_j} \left[\left(\mu + \frac{\mu_t}{\sigma_\epsilon} \right) \frac{\partial k}{\partial x_j} \right] + 2\mu_t s_{ij} s_{ij} - \rho \epsilon \quad (8)$$

$$\frac{\partial(\rho \epsilon)}{\partial t} + \frac{\partial(\rho \epsilon u_j)}{\partial x_j} = \frac{\partial}{\partial x_j} \left[\left(\mu + \frac{\mu_t}{\sigma_\epsilon} \right) \frac{\partial \epsilon}{\partial x_j} \right] + \rho C_1 \sqrt{2s_{ij}s_{ij}} \epsilon - \rho C_2 \frac{\epsilon^2}{k + \sqrt{\nu \epsilon}}, \quad (9)$$

where the closure coefficients and auxiliary relations are given by

$$C_1 = \max \left[0.43, \frac{\eta}{\eta + 5} \right], \eta = \sqrt{2s_{ij}s_{ij}} \frac{k}{\epsilon}, C_2 = 1.9, \sigma_k = 1.0, \sigma_\epsilon = 1.2.$$

The mean strain-rate tensor, s_{ij} , and the eddy viscosity, μ_t , are defined by

$$s_{ij} = \frac{1}{2} \left(\frac{\partial u_i}{\partial x_j} + \frac{\partial u_j}{\partial x_i} \right), \quad \mu_t = \rho C_\mu \frac{k^2}{\epsilon}$$

3. Two-equation non-linear (cubic) $k - \epsilon$ model equations :

$$\frac{\partial \bar{\rho} \tilde{k}}{\partial t} + \frac{\partial \bar{\rho} \tilde{u}_i \tilde{k}}{\partial x_i} = \frac{\partial}{\partial x_i} \left[\left(\mu + \frac{\mu_t}{\sigma_k} \right) \frac{\partial \tilde{k}}{\partial x_i} \right] + P_k - \bar{\rho} \tilde{\epsilon} \quad (10)$$

$$\frac{\partial \bar{\rho} \tilde{\epsilon}}{\partial t} + \frac{\partial \bar{\rho} \tilde{u}_i \tilde{\epsilon}}{\partial x_i} = \frac{\partial}{\partial x_i} \left[\left(\mu + \frac{\mu_t}{\sigma_\epsilon} \right) \frac{\partial \tilde{\epsilon}}{\partial x_i} \right] + (C_{\epsilon 1} P_k - [C_{\epsilon 2} \bar{\rho} \tilde{\epsilon} - E]) T_t^{-1}. \quad (11)$$

Where $P_k = -\bar{\rho} \widetilde{u''_i u''_j \frac{\partial \tilde{u}_i}{\partial x_j}}$ and $\bar{\rho} \widetilde{u''_i u''_j}$ is modeled by

$$\begin{aligned} \bar{\rho} \widetilde{u''_i u''_j} = & \bar{\rho} \frac{2}{3} \tilde{k} \delta_{ij} - \mu_t S_{ij}^* \\ & + c_1 \frac{\mu_t \tilde{k}}{\epsilon} \left(S_{ij}^* S_{kj}^* - \frac{1}{3} S_{kl}^* S_{kl}^* \delta_{ij} \right) \\ & + c_2 \frac{\mu_t \tilde{k}}{\epsilon} \left(\Omega_{ik} S_{kj}^* + \Omega_{jk} S_{ki}^* \right) \\ & + c_3 \frac{\mu_t \tilde{k}}{\epsilon} \left(\Omega_{ij} \Omega_{jk} - \frac{1}{3} \Omega_{lk} \Omega_{lk} \delta_{ij} \right) \\ & + c_4 \frac{\mu_t k^2}{\epsilon^2} \left(\Omega_{lj} S_{ki}^* + \Omega_{li} S_{kj}^* \right) S_{kl}^* \\ & + c_5 \frac{\mu_t \tilde{k}^2}{\epsilon^2} \left(\Omega_{il} \Omega_{lm} S_{mj}^* + \Omega_{lm} \Omega_{mj} S_{il}^* - \frac{2}{3} \Omega_{mn} \Omega_{nl} S_{lm}^* \delta_{ij} \right) \\ & + c_6 \frac{\mu_t k^2}{\epsilon^2} S_{ij}^* S_{kl}^* S_{kl}^* \\ & + c_7 \frac{\mu_t k^2}{\epsilon^2} S_{ij}^* \Omega_{kl} \Omega_{kl}. \end{aligned}$$

For above equation, the following relations are prescribed

$$S_{ij}^* = \left(\frac{\partial \tilde{u}_i}{\partial x_j} + \frac{\partial \tilde{u}_j}{\partial x_i} \right) - \frac{2}{3} \frac{\partial \tilde{u}_k}{\partial x_k} \delta_{ij}, \Omega_{ij} = \left(\frac{\partial \tilde{u}_i}{\partial x_j} - \frac{\partial \tilde{u}_j}{\partial x_i} \right), S = \frac{\tilde{k}}{\tilde{\epsilon}} \sqrt{\frac{1}{2} S_{ij}^* S_{ij}^*}, \Omega = \frac{\tilde{k}}{\tilde{\epsilon}} \sqrt{\frac{1}{2} \Omega_{ij}^* \Omega_{ij}^*}.$$

Time scale is defined as,

$$\tau = \frac{\tilde{k}}{\tilde{\epsilon}}, T_t = \tau \max\{1, \xi^{-1}\}, \text{ where } \xi = \frac{\sqrt{R_t}}{C_\tau}, \text{ with } R_t = \frac{\tilde{k}^2}{\nu \epsilon}, \text{ and } C_\tau = \sqrt{2}$$

Eddy viscosity is defined as $\mu_t = \frac{C_\mu f_\mu \bar{\rho} \tilde{k}^2}{\epsilon}$. The remaining model parameters are given by,

$$\begin{aligned} C_{\mu S Z L} &= \frac{2/3}{A_1 + S + 0.9\Omega}, & C_{\mu G} &= \min \left\{ \frac{0.09 + 0.13\phi}{1 + \phi^{2.5}}, C_{\mu S Z L} \right\}, & \phi &= |\Omega - S|, \\ c_1 &= \frac{3/4}{(1000 + S^3) C_\mu}, & c_2 &= \frac{15/4}{(1000 + S^3) C_\mu}, & c_3 &= \frac{-19/4}{(1000 + S^3) C_\mu}, \\ c_4 &= -10 C_\mu^2, & c_5 &= 0, & c_6 &= -2 C_\mu^2, c_7 &= -c_6 \\ f_\mu &= \frac{1 - e^{-A_\mu R_t}}{1 - e^{-\sqrt{R_t}}} \max\{1, \xi^{-1}\}, & E &= A_{E\tau} \bar{\rho} \max[\tilde{k}^{1/2}, (\nu \tilde{\epsilon})^{1/4}] \sqrt{\epsilon T} \Psi_\tau, & \Psi_\tau &= \max \left\{ \frac{\partial \tilde{k}}{\partial x_j} \frac{\partial \tau}{\partial x_j}, 0 \right\}. \end{aligned}$$

The model constants are being $A_1 = 1.25, C_{\epsilon 1} = 1.44, C_{\epsilon 2} = 1.92, \sigma_k = 1.0, \sigma_\epsilon = 1.3, A_\mu = 0.0085, A_{E\tau} = 0.15$, and $C_s = 0.05$.

4. Two-equation shear stress transport (SST) model: the Reynold's stresses are given by $\rho \bar{u}_i \bar{u}_j = \frac{2}{3} \delta_{ij} \rho k - \mu_t S_{ij}$, with the mean strain rate tensor as $S_{ij} = \left(\frac{\partial U_i}{\partial x_j} + \frac{\partial U_j}{\partial x_i} - \frac{2}{3} \frac{\partial U_k}{\partial x_k} \delta_{ij} \right)$. The eddy viscosity is defined as $\nu_t = a_1 k / \max\{a_1 \omega, SF_2\}$. Turbulence kinetic energy transport equation is

$$\frac{\partial \rho k}{\partial t} + \frac{\partial}{\partial x_j} (u_j \rho k) = \tilde{P}_k - \beta^* \rho k \omega + \nabla \cdot [(\mu + \sigma_k \mu_t) \nabla k]. \quad (12)$$

Turbulence inverse time-scale transport equation is

$$\frac{\partial \rho \omega}{\partial t} + \frac{\partial}{\partial x_j} (u_j \rho \omega) = \frac{\gamma}{\hat{\nu}_t} P_k - \beta^* \rho \omega^2 + \nabla \cdot [(\mu + \sigma_\omega \mu_t) \nabla \omega] + 2(1 - F_1) \rho \sigma_{\omega 2} \frac{1}{\omega} \nabla k \cdot \nabla \omega, \quad (13)$$

where the turbulence generation term is computed by $P_k = |!| \left[\mu_t \left(\frac{\partial U_i}{\partial x_j} + \frac{\partial U_j}{\partial x_i} + \frac{2}{3} \frac{\partial U_k}{\partial x_k} \delta_{ij} \right) - \frac{2}{3} \rho k \delta_{ij} \right] \frac{\partial U_i}{\partial x_j}$.

In the k -equation, the turbulence generation term is limited as $\tilde{P}_k = \min(P_k, 10\beta^* \rho k \omega)$. F_1 and F_2 are blending functions

$$F_1 = \tanh \left\{ \left\{ \min \left[\max \left(\frac{\sqrt{k}}{\beta^* \omega d}, \frac{500\nu}{d^2 \omega} \right), \frac{4\rho \sigma_{\omega 2} k}{CD_{k\omega} d^2} \right] \right\}^4 \right\},$$

where $CD_{k\omega} = \max(2\rho \sigma_{\omega 2} \frac{1}{\omega} \nabla k \cdot \nabla \omega, 10^{-10})$, and

$$F_2 = \tanh \left\{ \left[\max \left(\frac{2\sqrt{k}}{\beta^* \omega d}, \frac{500\nu}{d^2 \omega} \right) \right]^2 \right\}.$$

In general, it is blended as $\phi = \phi_1 F_1 + \phi_2 (1 - F_1)$ with ϕ being various model constants. To close the turbulence equations, model constants are required $\sigma_{k1} = 0.85$ (0.5 for baseline), $\sigma_{\omega 1} = 0.5$, $\beta_1 = 0.075$, $\gamma_1 = \frac{\beta_1}{\beta^*} - \frac{\sigma_{\omega 1} \kappa^2}{\sqrt{\beta^*}}$, $\sigma_{k2} = 1.0$, $\sigma_{\omega 2} = 0.856$, $\beta_2 = 0.0828$, $\beta^* = 0.09$, $\kappa = 0.41$, $a_1 = 0.31$, and $\gamma_2 = \frac{\beta_2}{\beta^*} - \frac{\sigma_{\omega 2} \kappa^2}{\sqrt{\beta^*}}$. Note that for the smooth wall B.C.'s with $y^+ < 3$, k and ω are specified as $k = 0$ and $\omega = 800 \frac{\nu}{(\nabla y_1)^2}$. The eddy viscosity for the new ω equation is limited by $\hat{\nu}_t = \max(\nu_t, 10^{-8})$.

- Seven-equation second moment closure model: The mass averaged Reynolds-stress-transport equations may be written in generic form as,

$$\frac{\partial \bar{\rho} \widetilde{u''_i u''_j}}{\partial t} + \frac{\partial \bar{\rho} \widetilde{u''_i u''_j} \tilde{u}_k}{\partial t} = P_{ij} + d_{ij} + \phi_{ij}^* - \epsilon_{ij}. \quad (14)$$

In the above equation, the stress-production tensor, P_{ij} , is

$$P_{ij} = - \left(\bar{\rho} \widetilde{u''_i u''_k} \frac{\partial \tilde{u}_j}{\partial x_k} + \bar{\rho} \widetilde{u''_j u''_k} \frac{\partial \tilde{u}_i}{\partial x_k} \right).$$

The turbulent diffusion term, d_{ij} , is modeled by

$$d_{ij} = \frac{\partial}{\partial x_k} \left(\tilde{\mu} \frac{\partial \widetilde{u''_i u''_j}}{\partial x_k} + 0.22 \frac{\bar{\rho} \tilde{k}}{\tilde{\epsilon}} \left[\widetilde{u''_k u''_l} \frac{\partial \widetilde{u''_i u''_j}}{\partial x_l} \right] \right) + \frac{d_{kk}^P \bar{\rho} \widetilde{u''_i u''_j}}{2\tilde{k}},$$

where the pressure diffusion is represented by

$$d_{kk}^P = -\frac{1}{\bar{\rho}} \left(\frac{\partial \bar{\rho} \bar{u}_k}{\partial x_k} \right)$$

with $\bar{\rho} \bar{u}_k = -\bar{\rho}(1 - A)(0.5d_k + 1.1d_k^A)(\tilde{\nu} \tilde{\epsilon} A A_2)^{\frac{1}{2}} C_{pd}$ and $C_{pd} = \left[1 + 2e\left(-\frac{Re_t}{40}\right) \right] A_2 + 0.4 Re_t^{-\frac{1}{4}} e\left(-\frac{Re_t}{40}\right)$. In the preceding equations, the gradient-indicator vectors are

$$d_i = \frac{N_i}{[0.5 + \sqrt{N_k N_k}]}, \quad d_i^A = \frac{N_i^A}{[0.5 + \sqrt{N_k^A N_k^A}]}, \text{ where } N_i = \frac{\partial(lA)}{\partial x_i}, N_i^A = \frac{\partial(l\sqrt{A})}{\partial x_i}, l = \frac{\tilde{k}^{\frac{3}{2}}}{\tilde{\epsilon}}.$$

The dissipation rate tensor, ϵ_{ij} , is

$$\epsilon_{ij} = \frac{(1 - f_\epsilon) \bar{\rho} (\epsilon'_{ij} + \epsilon''_{ij})}{D + \frac{2}{3} f_\epsilon \bar{\rho} \tilde{\epsilon} \delta_{ij}}.$$

Terms in the above equation are given by

$$\begin{aligned}\epsilon'_{ij} &= \tilde{\epsilon} \frac{\widetilde{u''_i u''_j}}{\tilde{k}} + 2\nu \frac{\widetilde{u''_l u''_n}}{\tilde{k}} \frac{\partial \sqrt{\tilde{k}}}{\partial x_l} \frac{\partial \sqrt{\tilde{k}}}{\partial x_n} \delta_{ij} + 2\nu \left(\frac{\widetilde{u''_l u''_i}}{\tilde{k}} \frac{\partial \sqrt{\tilde{k}}}{\partial x_j} \frac{\partial \sqrt{\tilde{k}}}{\partial x_l} + \frac{\widetilde{u''_l u''_j}}{\tilde{k}} \frac{\partial \sqrt{\tilde{k}}}{\partial x_i} \frac{\partial \sqrt{\tilde{k}}}{\partial x_l} \right), \\ \epsilon''_{ij} &= f_R \tilde{\epsilon} \left[\frac{\widetilde{u''_l u''_k}}{\tilde{k}} d_l^A d_k^A \delta_{ij} - \frac{\widetilde{u''_l u''_i}}{\tilde{k}} d_l^A d_j^A - \frac{\widetilde{u''_l u''_j}}{\tilde{k}} d_l^A d_i^A \right], \\ D &= \frac{\epsilon'_{ij} + \epsilon''_{ij}}{2\tilde{\epsilon}} f_R = (1 - A) \min \left[\left(\frac{Re_t}{80} \right)^2, 1 \right], f_\epsilon = A^{\frac{1}{2}}.\end{aligned}$$

The equation for the homogeneous dissipation rate $\tilde{\epsilon}^*$ is

$$\begin{aligned}\frac{\partial \rho \tilde{\epsilon}^*}{\partial t} + \frac{\partial \rho \tilde{\epsilon}^* \tilde{u}_k}{\partial x_k} &= \frac{\partial}{\partial x_l} \left[\left(\tilde{\mu} \delta_{lk} + C_\epsilon \bar{\rho} \widetilde{u''_l u''_k} \frac{\tilde{k}}{\tilde{\epsilon}} \right) \frac{\partial \tilde{\epsilon}^*}{\partial x_k} \right] + \frac{C_{\epsilon 1} \bar{\rho} P_k}{\tau} - \frac{C_{\epsilon 2} \bar{\rho} \tilde{\epsilon}^*}{\tau}. \\ - \frac{C_{\epsilon 3} (\tilde{\epsilon} - \tilde{\epsilon}^*) \bar{\rho} \tilde{\epsilon}^*}{\tau} + C_{\epsilon 4} \tilde{\mu} \tau \widetilde{u''_i u''_j} \frac{\partial^2 \tilde{u}_k}{\partial x_i \partial x_l} \frac{\partial^2 \tilde{u}_k}{\partial x_j \partial x_l} &+ \frac{C_{\epsilon 5} \bar{\rho} \tilde{\epsilon}^*}{\tau} Y_P.\end{aligned}$$

Where

$$Y_P = 0.2 \min \{ \max[F(F+1)^2, 0], 20 \}$$

$$F = \left[\sqrt{\left(\frac{\partial l}{\partial x_j} \right) \left(\frac{\partial l}{\partial x_j} \right)} - \frac{\partial l_e}{\partial Y} \right] / c_l$$

$$\frac{\partial l_e}{\partial Y} = c_l [1 - e^{(-B_\epsilon Re_t)} + B_\epsilon Re_t e^{(-B_\epsilon Re_t)}]$$

$$c_l = 2.55, \quad B_\epsilon = 0.1069, \quad \tau = \frac{\tilde{k}}{\tilde{\epsilon}},$$

$$C_{\epsilon 1} = 1.44, \quad C_{\epsilon 2} = 1.92, \quad C_{\epsilon 3} = 1.0,$$

$$C_{\epsilon 4} = 0.4, \quad C_{\epsilon 5} = 0.2, \quad C_\epsilon = 0.18,$$

$$A \equiv \text{Lumley's stress-flatness parameter}, 1 - 9/8(A_2 - A_3)$$

$$A_2 \equiv \text{second invariant of stress-anisotropy tensor}, a_{ij} a_{ij}$$

$$A_3 \equiv \text{third invariant of stress-anisotropy tensor}, a_{ij} a_{jk} a_{ki}$$

$$a_{ij} \equiv \text{dimensionless stress-anisotropy tensor}, \widetilde{u''_i u''_j} / \tilde{k} - 2\delta_{ij}/3$$

$$d_i, d_i^A \equiv \text{normalized direction indicator vectors}$$

$$d_{ij} \equiv \text{diffusive transport of } \widetilde{u''_i u''_j}$$

$$d_{ij}^P \equiv \text{diffusive transport of } \widetilde{u''_i u''_j} \text{ due to pressure fluctuations}$$

$$k \equiv \text{mass averaged turbulent kinetic energy}$$

$$N_i, N_i^A \equiv \text{length-scale and modified length-scale-gradient vectors}$$

$$P_{ij} \equiv \text{stress-production tensor}$$

$$\widetilde{Re_t} \equiv \text{turbulent Reynolds number}, \frac{\tilde{k}}{\tilde{\nu} \tilde{\epsilon}}$$

$$\widetilde{u''_i u''_j} \equiv \text{Reynolds averaged Reynolds stress tensor}$$

$$\delta_{ij} \equiv \text{Kronecker delta}$$

$$\epsilon_{ij} \equiv \text{dissipation rate of } \widetilde{u''_i u''_j}$$

$$\tilde{\epsilon} \equiv \text{dissipation rate of } \tilde{k}, \tilde{\epsilon}^* + 2\nu \left(\frac{\partial \tilde{k}^{\frac{1}{2}}}{\partial x_j} \right)^2$$

$$\tilde{\epsilon}^* \equiv \text{homogeneous dissipation rate of } \tilde{k}$$

$$\phi_{ij}^* \equiv \text{modified pressure strain tensor}$$

6. Hellsten quartic $k - \omega$ model: The eddy viscosity is defined as

$$\mu_t = \frac{a_1 \rho k}{\max(a_1 \omega; |S_{ij}| F_2 F_3)},$$

where a_1 is the Bradshaw's structural parameter, $F_2 = \tanh(\Gamma_2^2)$, where $\Gamma_2 = \max\left(\frac{2\sqrt{k}}{\beta^* \omega d}; \frac{500\nu}{\omega d^2}\right)$ and $F_3 = 1 - \tanh\left[\left(\frac{150\nu}{\omega d^2}\right)^4\right]$.

The $k - \omega$ transport equations are

$$\frac{\partial(\rho k)}{\partial t} + \frac{\partial}{\partial x_j}(U_j \rho k) = \frac{\partial}{\partial x_j} \left[(\mu + \sigma_k \mu_t) \frac{\partial k}{\partial x_j} \right] + P - \beta^* \rho k \omega, \quad (15)$$

$$\frac{\partial(\rho \omega)}{\partial t} + \frac{\partial}{\partial x_j}(U_j \rho \omega) = \frac{\partial}{\partial x_j} \left[(\mu + \sigma_\omega \mu_t) \frac{\partial \omega}{\partial x_j} \right] + \frac{\gamma \rho}{\mu_T} P - F_4 \beta \rho \omega^2 + 2\rho \frac{1 - F_1}{\sigma_{\omega 2} \omega} \frac{\partial k}{\partial x_j} \frac{\partial \omega}{\partial x_j}. \quad (16)$$

The turbulence generation term, the strain-rate tensor, F_1 , and F_4 are given by

$$P = \left(2\mu_T S_{ij} - \frac{2}{3} \delta_{ij} \rho k \right) \frac{\partial u_i}{\partial x_j}, \quad S_{ij} = \frac{1}{2} \left(\frac{\partial u_i}{\partial x_j} + \frac{\partial u_j}{\partial x_i} \right), \quad F_1 = \tanh(\Gamma^4), \quad F_4 = \frac{1}{1 + C_{rc} Ri}.$$

For the above auxiliary relations, coefficients are prescribed $\Gamma = \min\left(\max\left(\frac{\sqrt{k}}{\beta^* \omega d}; \frac{500\nu}{\omega d^2}\right); \frac{4\rho \sigma_{\omega 2} k}{CD_{k\omega} d^2}\right)$, $CD_{k\omega} = \max\left(\frac{2\rho}{\sigma_{\omega 2} \omega} \frac{\partial k}{\partial x_j} \frac{\partial \omega}{\partial x_j}; CD_{k\omega \min}\right)$, and C_{rc} is the constant coefficient in the rotation and curvature sensitization. The Richardson number is defined as

$$Ri = \frac{|\Omega_{ij}|}{|S_{ij}|} \left(\frac{|\Omega_{ij}|}{|S_{ij}|} - 1 \right) \text{ with vorticity tensor } \Omega_{ij} = \left(\frac{\partial u_i}{\partial x_j} - \frac{\partial u_j}{\partial x_i} \right) / 2.$$

The scalar measure of vorticity tensor is $|\Omega_{ij}| = \sqrt{2\Omega_{ij}\Omega_{ij}}$ and the same with the scalar measure of the strain rate tensor. Model constants include

$$\gamma = \frac{\beta}{\beta^*} - \frac{\sigma_\omega \kappa^2}{\sqrt{\beta^*}}$$

and $\beta_1 = 0.075, \beta_2 = 0.0828, \sigma_{k1} = 0.5, \sigma_{k2} = 1.0, \sigma_{\omega 1} = 0.5, \sigma_{\omega 2} = 0.856, \beta^* = 0.09$, and $\kappa = 0.41$.

Hellsten's $k - \omega$ model differs from Menter's in its definition of $CD_{k\omega}$ (the positive portion of the cross-diffusion in the ω transport equation). In the original model the second term was 10^{-20} . In Menter's 2003 version it was amended to be 10^{-10} , and in Hellsten's model the second term was redefined to be 10^{-8} multiplied by the maximum value of the cross diffusion term found in the flow field. A simpler, but less accurate, approximation of this term can be found using the maximum value in each grid block as opposed to the flow field as a whole.

VII.B. Grid Refinement Study

We conducted a grid refinement study using the Spalart-Allmaras model on a series of consecutively coarsened grids. The figures below are identical to those shown for the comparison of the turbulence models, but are for results using a single model on multiple grids.

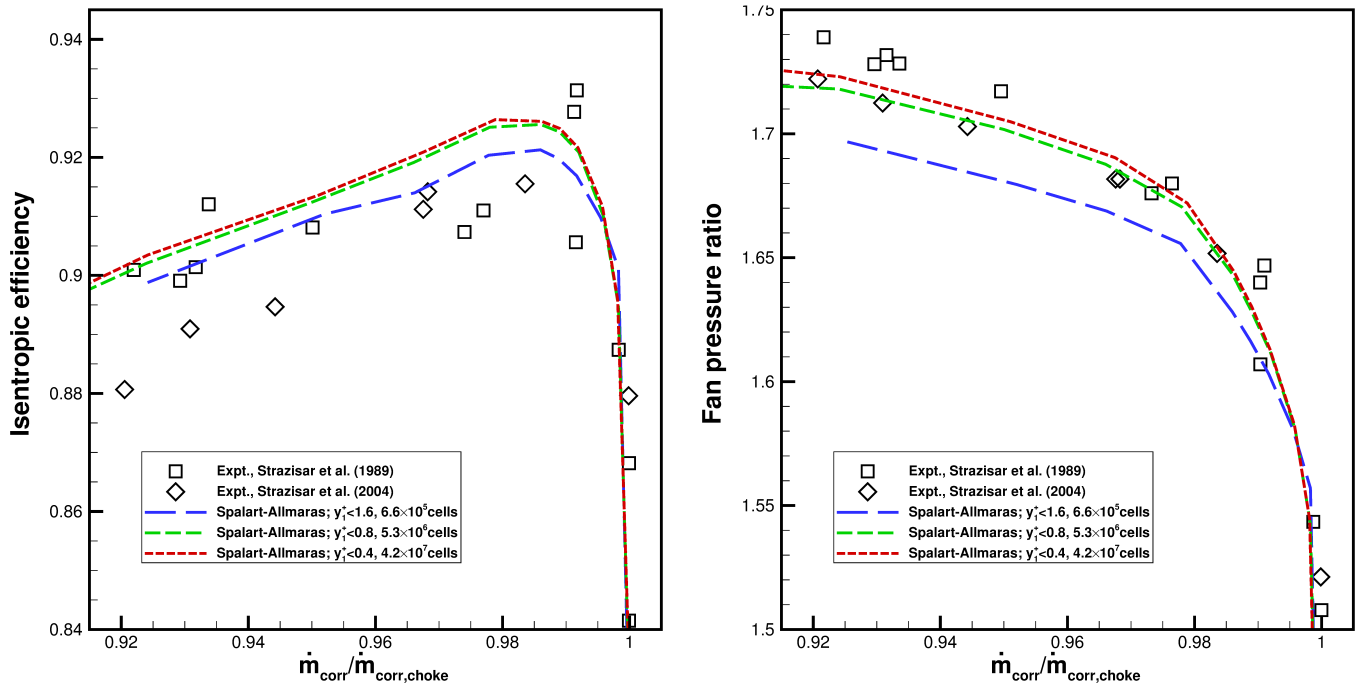


Figure 11: Efficiency and FPR

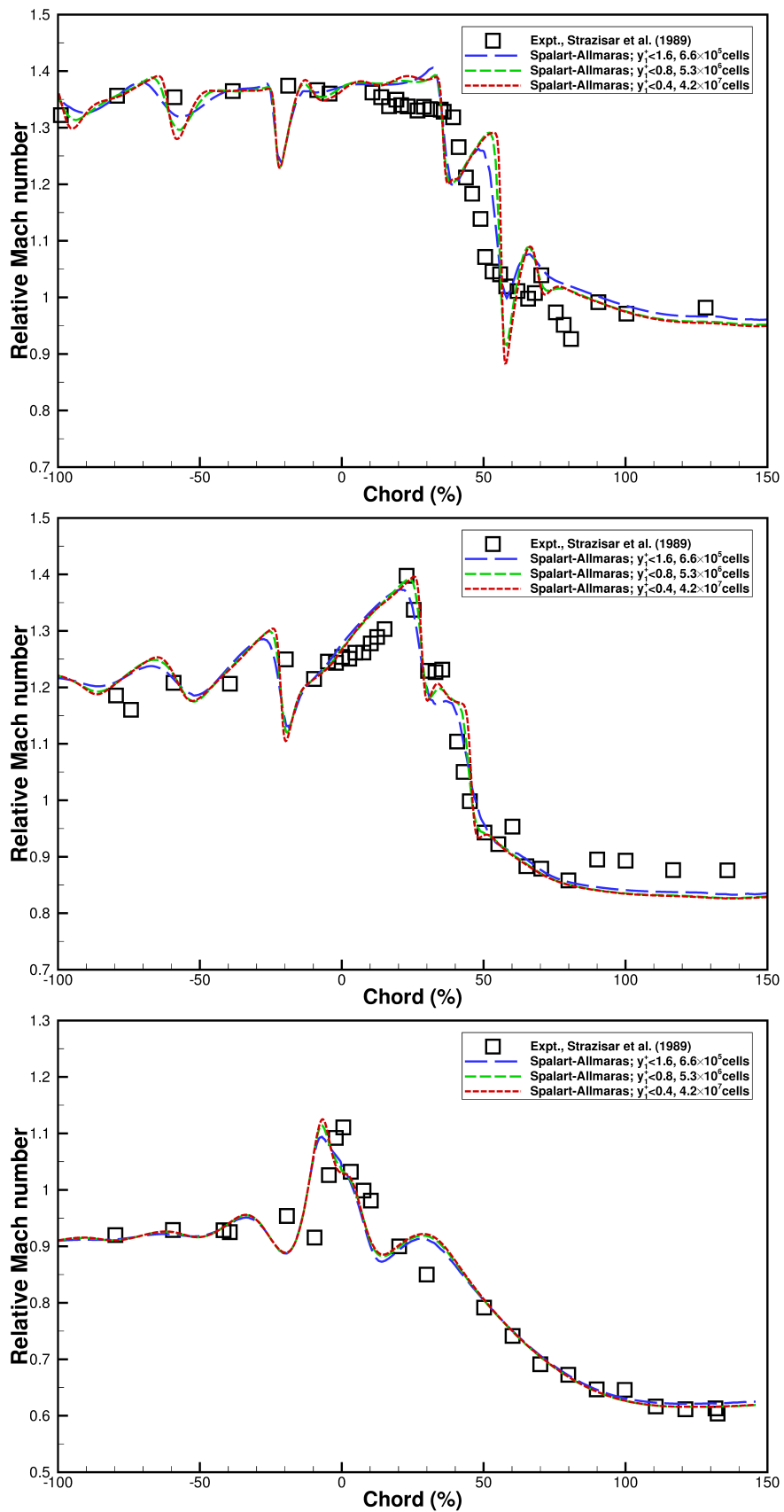


Figure 12: Relative Mach number at 90% span (top), 70% span (middle), and 30% span (bottom) from the hub and at 50% pitch, for the rotor alone operating near peak efficiency.

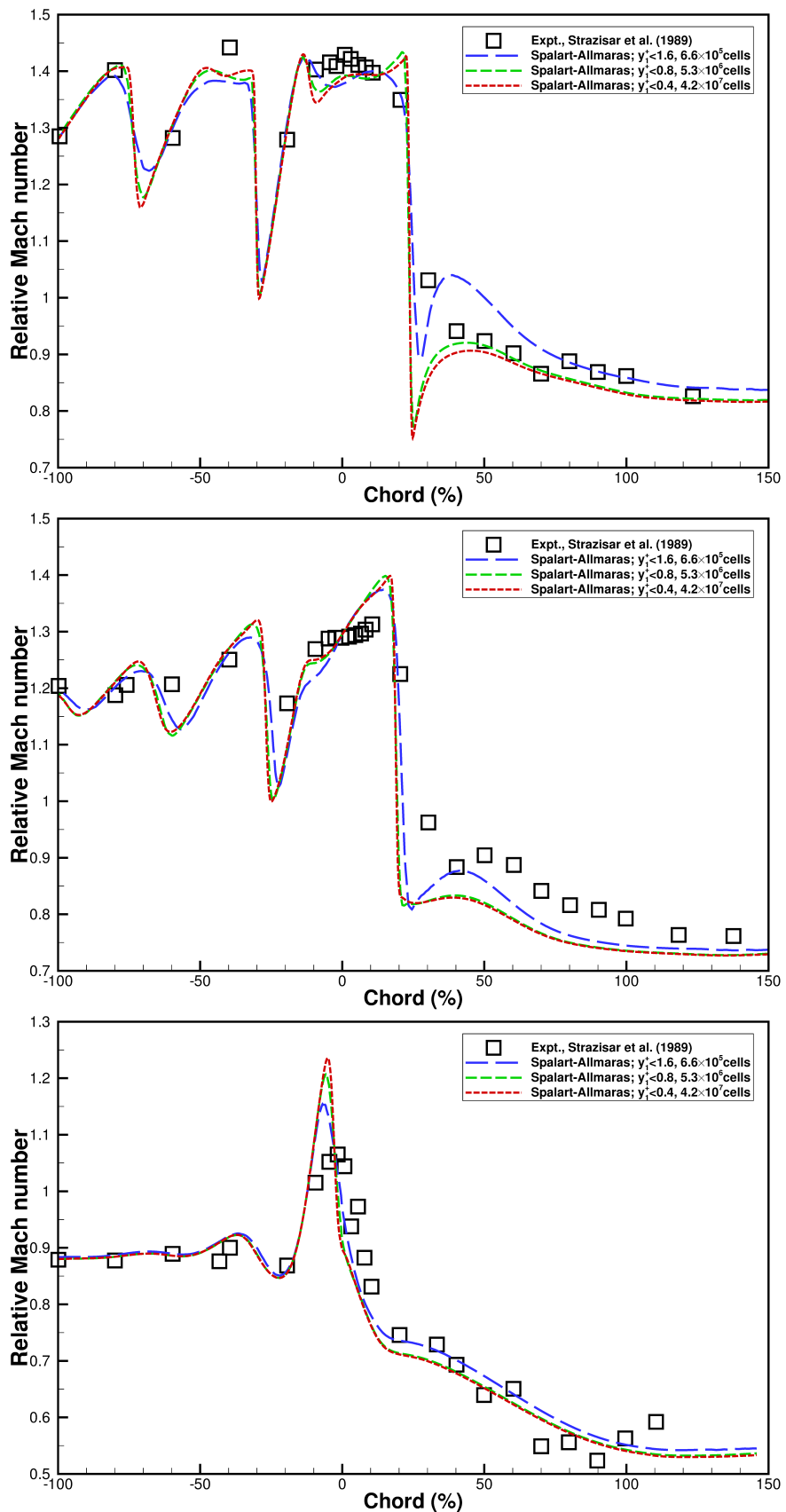


Figure 13: Relative Mach number at 90% span (top), 70% span (middle), and 30% span (bottom) from the hub and at 50% pitch, for the rotor alone operating near stall.

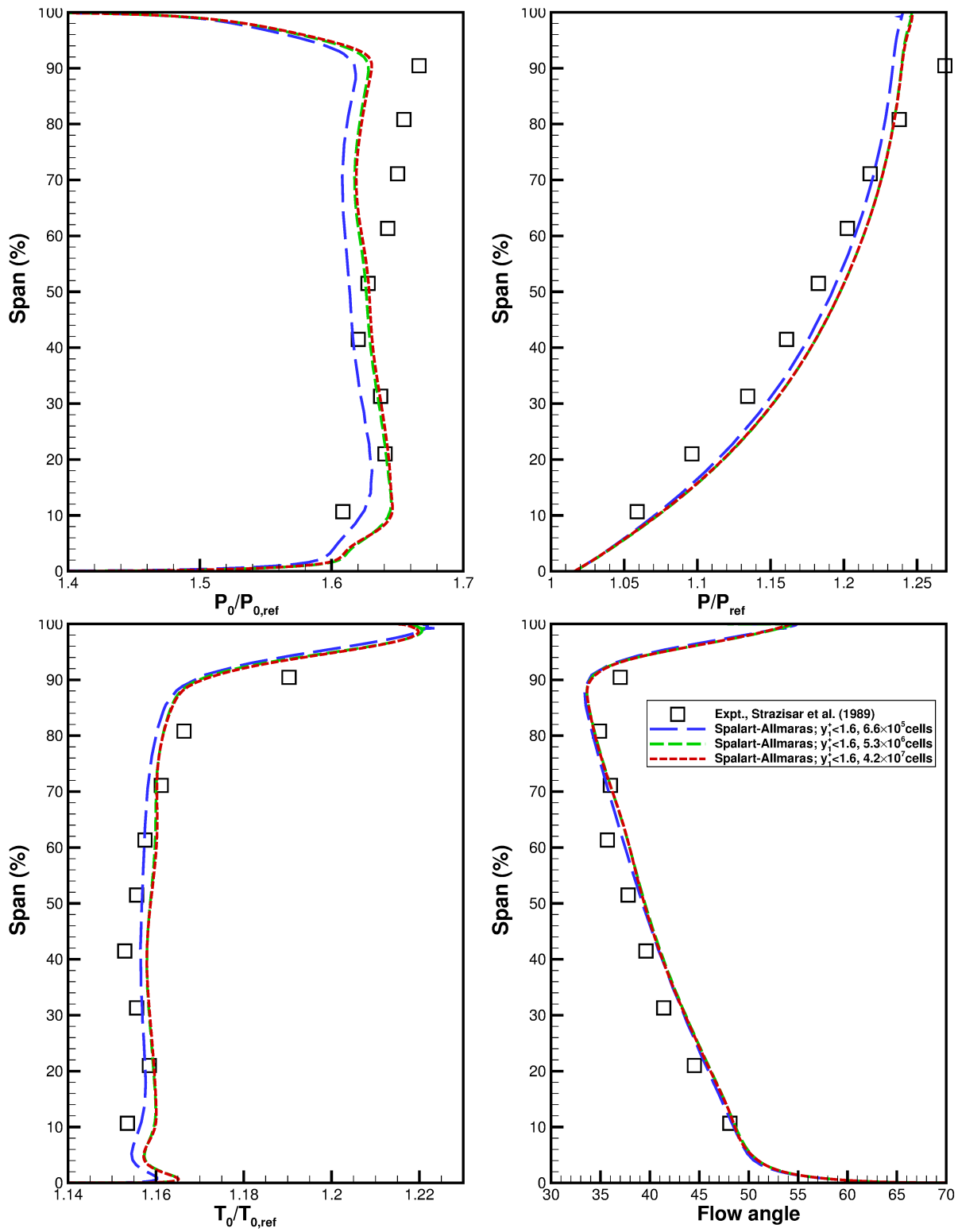


Figure 14: Spanwise distributions of total pressure (top-left), total temperature (top-right), static pressure (bottom-left), and exit flow angle (bottom-right) for the rotor alone operating near peak efficiency

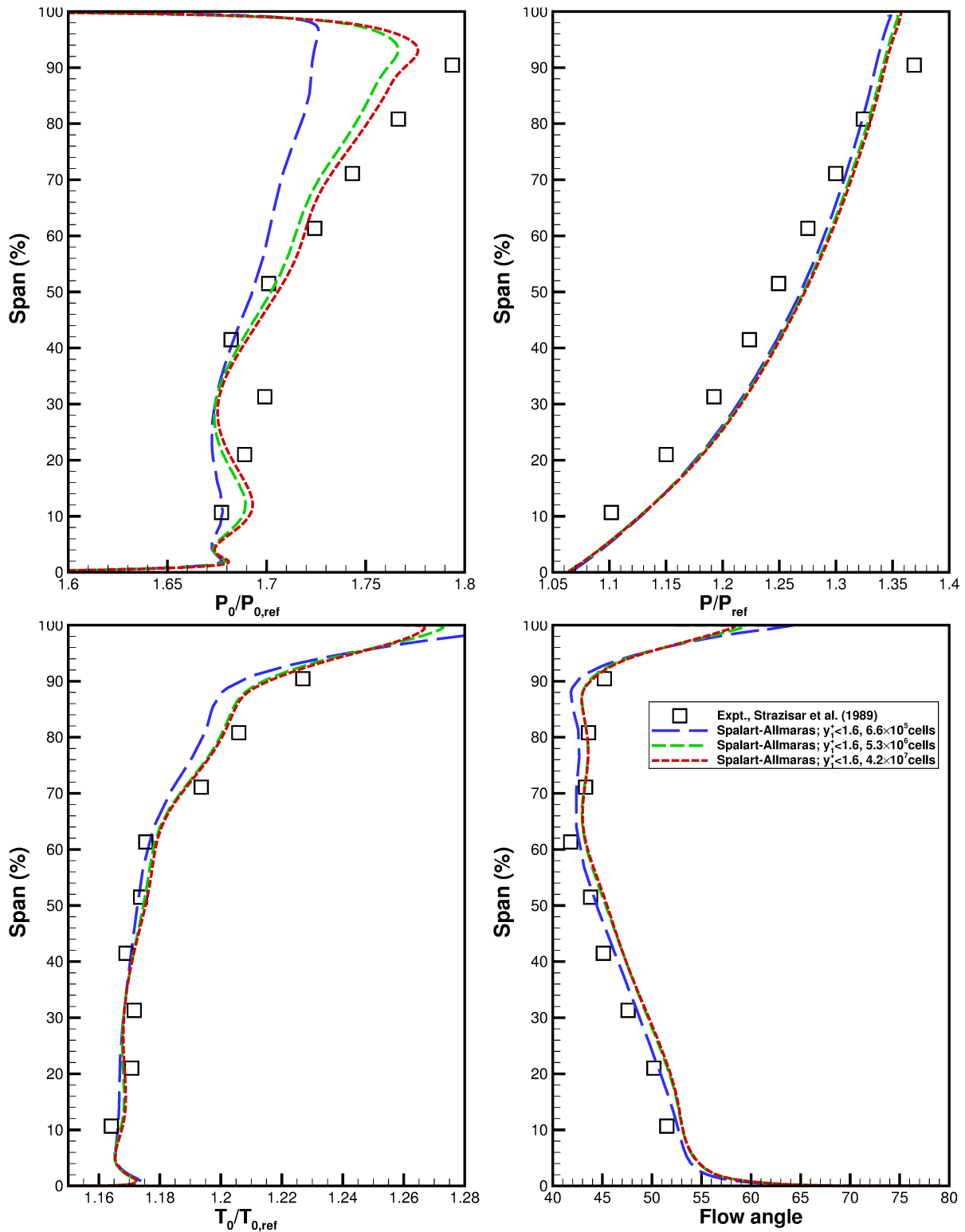


Figure 15: Spanwise distributions of total pressure (top-left), total temperature (top-right), static pressure (bottom-left), and exit flow angle (bottom-right) for the rotor alone operating near peak efficiency

References

- ¹Hinze, J. O., *Turbulence*, McGraw-Hill, 2nd ed., 1975.
- ²Jennions, I. K. and Turner, M. G., "Three-Dimensional Navier-Stokes Computations of Transonic Fan Flow Using an Explicit Flow Solver and an Implicit $k - \epsilon$ Solver," *Journal of Turbomachinery*, Vol. 115, No. 2, Apr 1993, pp. 261-272.
- ³Hellsten, A., "Some Improvements in Menter's $k - \omega$ SST Turbulence Model," No. AIAA-98-2554, June 1998.
- ⁴Tsuei, H. and Perot, J. B., "Advanced Turbulence Model for Transitional and Rotational Flows in Turbomachinery," Paper 2000-0134, American Institute of Aeronautics and Astronautics, 2000.
- ⁵Jakirlić, S., Hanjalić, K., and Tropea, C., "Modeling Rotating and Swirling Turbulent Flows: A Perpetual Challenge," *AIAA J*, Vol. 40, No. 10, October 2002.
- ⁶Gunderson, T. O. K., *Modelling of Rotating Turbulent Flows*, Master's thesis, Norwegian University of Science and Technology, 2011.
- ⁷von Lavante, E. and Yao, J., "Numerical Investigation of Turbulent Swirling Flows in Axisymmetric Internal Flow Configurations," *Flow Measurement and Instrumentation*, Vol. 25, 1983, pp. 63-68.
- ⁸Wilcox, D. M., *Turbulence Modeling for CFD Second Edition*, DCW Industries Inc., 1998.
- ⁹Goldberg, U., O., P., and Chakravarthy, S., "A Wall-Distance-Free $k - \epsilon$ Model With Enhanced Near-Wall Treatment," *ASME JFE*, Vol. 120, 1998, pp. 457-462.
- ¹⁰He, C., Corke, T., and Patel, M., "Numerical and Experimental Analysis of Plasma Flow Control Over a Hump Model," No. 2007-0935, 45th Aerospace Sciences Meeting, Reno, Nevada, January 2007.
- ¹¹Palaniswamy, S., Goldberg, U., Peroomian, O., and Chakravarthy, S., "Predictions of Axial and Transverse Injection into Supersonic Flow," *Turbulence and Combustion*, , No. 66, 2001, pp. 37-55.
- ¹²J., C. T. and E., L. B., "A Reynolds stress closure designed for complex geometries," *Int. J. Heat Fluid Flow*, , No. 17, 1996, pp. 245-254.
- ¹³P., B., J., C. T., and H., L. M. A. L., "Reynolds-stress-transport modeling for compressible aerodynamics applications," *AIAA J*, Vol. 37, 1999.
- ¹⁴Chima, R. V., "Viscous Three-Dimensional Calculations of Transonic Fan Performance," Technical Memorandum 103800, NASA, 1991.
- ¹⁵Strazisar, A. J., Wood, J. R., Hathaway, M. D., and Suder, K. L., "Laser Anemometer Measurements in a Transonic Axial-flow Fan Rotor," Technical Paper 2879, NASA, Cleveland, Ohio, Nov 1989.
- ¹⁶Hah, C. and Reid, L., "A Viscous Flow Study of Shock-Boundary Layer Interaction, Radial Transport, and Wake Development in a Transonic Compressor," *Journal of Turbomachinery*, Vol. 114, No. 3, June 1992, pp. 538-547.
- ¹⁷Grosvenor, A. D., "RANS Prediction of Transonic Compressive Rotor Performance Near Stall," *Proceedings of ASME Turbo Expo 2007: Power for Land, Sea, and Air*, ASME, May 2007.
- ¹⁸Grosvenor, A. D., "Numerical Studies Toward Prediction, Analysis and Treatment of SWBLI in Transonic Compressors," *Proceedings of the International Conference on the Methods of Aerophysical Research*, 2008.
- ¹⁹Fidalgo, V. J., Hall, C. A., and Colin, Y., "A Study of Fan-Distortion Interaction Within the NASA Rotor 67 Transonic Stage," *Journal of Turbomachinery*, Vol. 134, No. 5, 2012.
- ²⁰Adamczyk, J. D., "Model Equation for Simulating Flows in Multistage Turbomachinery," *Proceedings of ASME Gas Turbine Conference and Exhibit*, ASME, March 1985.
- ²¹Urasek, D. C., Gorrel, W. T., and Cunnan, W. S., "Performance of Two-Stage Fan Having Low-Aspect-Ratio, First-Stage Rotor Blading," Technical Paper 1493, NASA, 1979.
- ²²Cunnan, W. S., Stevans, W., and Urasek, D. C., "Design and Performance of a 427-Meter-Per-Second-Tip-Speed Two-Stage Fan Having a 2.40 Pressure Ratio," Technical Paper 1314, NASA, 1978.
- ²³Hathaway, M. D., "Unsteady Flows in a Single-Stage Transonic Axial-Flow Fan Stator Row," Technical Memorandum 88929, NASA, Cleveland, Ohio, Dec 1986.
- ²⁴Suder, K. L., Hathaway, M. D., Okiishi, T. H., Strazisar, A. J., and Adamczyk, J. J., "Measurements of the Unsteady Flow Field Within the Stator Row of a Transonic Axial-Flow Fan: I - Measurement and Analysis Technique," Technical Memorandum 88945, NASA, Cleveland, Ohio, Dec 1987.
- ²⁵Hathaway, M. D., Suder, K. L., Okiishi, T. H., Strazisar, A. J., and Adamczyk, J. J., "Measurements of the Unsteady Flow Field Within the Stator Row of a Transonic Axial-Flow Fan: II - Results and Discussion," Technical Memorandum 88946, NASA, Cleveland, Ohio, Dec 1987.
- ²⁶"<http://www.metacomptech.com/> .